The Astrophysical Journal, 953:10 (13pp), 2023 August 10 https://doi.org/10.3847/1538-4357/acde55

Using [Ne V]/[Ne III] to Understand the Nature of Extreme-ionization Galaxies

Nikko J. Cleri[1,2], Grace M. Olivier[1,2], Taylor A. Hutchison[3,15], Casey Papovich[1,2], Jonathan R. Trump[4], Ricardo O. Amorín[5,6], Bren E. Backhaus[4], Danielle A. Berg[7], Vital Fernández[5], Steven L. Finkelstein[7], Seiji Fujimoto[8,9], Michaela Hirschmann[10], Jeyhan S. Kartaltepe[11], Dale D. Kocevski[12], Raymond C. Simons[4], Stephen M. Wilkins[13,14], and L. Y. Aaron Yung[3,15]

[1] Department of Physics and Astronomy, Texas A&M University, College Station, TX 77843-4242, USA; cleri@tamu.edu
[2] George P. and Cynthia Woods Mitchell Institute for Fundamental Physics and Astronomy, Texas A&M University, College Station, TX 77843-4242, USA
[3] Astrophysics Science Division, NASA Goddard Space Flight Center, 8800 Greenbelt Rd, Greenbelt, MD 20771, USA
[4] Department of Physics, University of Connecticut, 196 Auditorium Road, Unit 3046, Storrs, CT 06269, USA
[5] Instituto de Investigación Multidisciplinar en Ciencia y Tecnología, Universidad de La Serena, Raul Bitrán 1305, La Serena 2204000, Chile
[6] Departamento de Astronomía, Universidad de La Serena, Av. Juan Cisternas 1200 Norte, La Serena 1720236, Chile
[7] Department of Astronomy, The University of Texas, Austin, TX 78712, USA
[8] Cosmic Dawn Center (DAWN), Jagtvej 128, DK-2200 Copenhagen N, Denmark
[9] Niels Bohr Institute, University of Copenhagen, Lyngbyvej 2, DK-2100 Copenhagen Ø, Denmark
[10] Institute of Physics, Laboratory of Galaxy Evolution, EPFL, Observatoire de Sauverny, 1290 Versoix, Switzerland
[11] Laboratory for Multiwavelength Astrophysics, School of Physics and Astronomy, Rochester Institute of Technology, 84 Lomb Memorial Drive, Rochester, NY 14623, USA
[12] Department of Physics and Astronomy, Colby College, Waterville, ME 04901, USA
[13] Astronomy Centre, University of Sussex, Falmer, Brighton, BN1 9QH, UK
[14] Institute of Space Sciences and Astronomy, University of Malta, Msida, MSD 2080, Malta

Received 2023 January 23; revised 2023 June 8; accepted 2023 June 12; published 2023 July 28

Abstract

Spectroscopic studies of extreme-ionization galaxies (EIGs) are critical to our understanding of exotic systems throughout cosmic time. These EIGs exhibit spectral features requiring >54.42 eV photons: the energy needed to ionize helium into He^{2+} fully and emit He II recombination lines. Spectroscopic studies of EIGs can probe exotic stellar populations or accretion onto intermediate-mass black holes ($\sim 10^2$–10^5 $M_\odot$), which are the possibly key contributors to the reionization of the Universe. To facilitate the use of EIGs as probes of high-ionization systems, we focus on ratios constructed from several rest-frame UV/optical emission lines: [O III] λ5008, Hβ, [Ne III] λ3870, [O II] $\lambda\lambda$3727, 3729, and [Ne V] λ3427. These lines probe the relative intensity at energies of 35.12, 13.62, 40.96, 13.62, and 97.12 eV, respectively, covering a wider range of ionization than traced by other common rest-frame UV/optical techniques. We use the ratios of these lines ([Ne V]/[Ne III] $\equiv$ Ne53, [O III]/Hβ, and [Ne III]/[O II]), which are nearby in wavelength, mitigating the effects of dust attenuation and uncertainties in flux calibration. We make predictions from photoionization models constructed from `Cloudy` that use a broad range of stellar populations and black hole accretion models to explore the sensitivity of these line ratios to changes in the ionizing spectrum. We compare our models to observations from the Hubble Space Telescope and JWST of galaxies with strong high-ionization emission lines at $z \sim 0$, $z \sim 2$, and $5 < z < 8.5$. We show that the Ne53 ratio can separate galaxies with ionization from "normal" stellar populations from those with active galactic nuclei and even "exotic" Population III models. We introduce new selection methods to identify galaxies with photoionization driven by Population III stars or intermediate-mass black hole accretion disks that could be identified in upcoming high-redshift spectroscopic surveys.

Unified Astronomy Thesaurus concepts: Active galaxies (17); Reionization (1383); Black Holes (162); Intermediate-mass Black Holes (816); Population III stars (1285); Stellar populations (1622); Photoionization (2060); Galaxy evolution (594); Interstellar medium (847); Active galactic nuclei (16); High-redshift galaxies (734)

1. Introduction

Emission-line spectroscopy provides a wealth of information about the physical conditions of a galaxy. From a rest-frame ultraviolet (UV)/optical spectrum of a galaxy, we can discern its chemical abundance and metallicity (e.g., Lequeux et al. 1979), star formation rate (e.g., Kennicutt 1998; Kennicutt & Evans 2012), nebular dust attenuation estimates (e.g., Buat et al. 2002; Groves et al. 2012), temperature and density of the interstellar medium (ISM; e.g., Dopita et al. 2000; Kewley et al. 2019; Maiolino & Mannucci 2019), and any contribution from an active galactic nucleus (AGN) to the emission (e.g., Baldwin et al. 1981; Veilleux & Osterbrock 1987; Trump et al. 2015). Much of the knowledge of these physical properties of a galaxy's ionized gas is derived from bright Balmer lines of hydrogen (Hα and Hβ), along with metal lines from oxygen ([O II] $\lambda\lambda$3727, 3729 and [O III] $\lambda\lambda$4960, 5008), sulfur ([S II] $\lambda\lambda$6718, 6733), and nitrogen ([N II] λ 6585),[16] while P Cygni stellar wind features characterize the massive star population.

---

[15] NASA Postdoctoral Fellow.

[16] Vacuum wavelengths.

Historically, studies of emission-line galaxies use ratios of emission-line fluxes with small wavelength separations as a way to minimize uncertainties. Commonly used emission-line ratios in the UV and optical such as [O III] $\lambda5008/\mathrm{H}\beta$, [Ne III] $\lambda3870$/[O II] $\lambda3728$, [N II] $\lambda6585/\mathrm{H}\alpha$, and [S II] $\lambda6718/\mathrm{H}\alpha$, are relatively insensitive to dust attenuation and spectral calibrations, and as such are very useful tracers of ISM and AGN narrow-line region (NLR) conditions (e.g., Baldwin et al. 1981; Veilleux & Osterbrock 1987).

These rest-frame UV and optical emission-line ratios are tools for understanding how H-ionizing photons (Lyman continuum photons with $\lambda < 912$ Å) escaped from high-redshift galaxies. As such, this is paramount at $z > 6$ as this radiation is the most likely candidate for reionizing the Universe (e.g., Finkelstein et al. 2015). Currently, few studies have successfully employed these UV and optical lines at $z > 6$ during this so-called epoch of reionization (EoR), thus the physical nature of the ionizing spectra and physical properties of the galaxies responsible remain poorly understood. With the advent of the JWST era, we now have unprecedented access to spectroscopic observations of these early Universe systems. JWST's Near-Infrared Spectrograph (NIRSpec) coverage spans 0.6–5.3 μm, allowing detection of rest-frame UV and optical emission lines well into the EoR, with spectral resolutions ($R \sim 1000$ or $R \sim 2700$, depending on the observing mode) easily capable of resolving important emission features for these studies.

The chemically young and highly energetic stellar populations in galaxies during the EoR are expected to be key contributors to the hydrogen reionization of the Universe (e.g., Zackrisson et al. 2011; Finkelstein et al. 2015; Berg et al. 2016, 2019, 2021; Brinchmann 2023; Curtis-Lake et al. 2023; Trussler et al. 2022; Trump et al. 2023). These objects show prominent high-ionization ($\gtrsim$35 eV creation potential; Berg et al. 2021) emission lines, suggesting that they are characterized by hard radiation fields (Smit et al. 2014; Stark 2016; Katz et al. 2023b; Brinchmann 2023; Trump et al. 2023).

Previous studies of high-ionization emission-line galaxies (ELGs) have focused primarily on spectral features in the Berg et al. (2021) "high-ionization regime," including C IV $\lambda\lambda1548$, 1551, [Ne III] $\lambda3870$, [O III] $\lambda\lambda4960$, 5008, He II $\lambda1640$, He II $\lambda4687$, and [Ar IV] $\lambda\lambda4712$, 4741 (e.g., Atek et al. 2011; van der Wel et al. 2011; Maseda et al. 2013; Levesque & Richardson 2014; Maseda et al. 2014; Masters et al. 2014; Amorín et al. 2015; Kehrig et al. 2015; Rigby et al. 2015; Zeimann et al. 2015; Berg et al. 2016; Amorín et al. 2017; Senchyna et al. 2017; Kehrig et al. 2018; Berg et al. 2019; Tang et al. 2019; Senchyna et al. 2020; Berg et al. 2021; Kehrig et al. 2021; Pérez-Montero et al. 2021; Tang et al. 2021; Backhaus et al. 2022; Olivier et al. 2022). Several studies have already suggested that chemically evolved Population I and II stars are unable to account for the strength of emission in the highest-energy lines, and instead they require additional sources of (hard) ionizing spectra (e.g., Steidel et al. 2014; Olivier et al. 2022).

Such systems, which we dub "extreme-ionization galaxies" (EIGs), exhibit spectral features which require radiation hard enough to ionize helium fully (>54.42 eV). These galaxies often require harder ionization than produced from "normal" stellar populations to produce such high-energy emission features. Such ionizing sources may be more exotic than "normal" stellar populations, including accreting massive black holes (BHs), supernovae, Population III stars, Wolf–Rayet stars, stripped stars in binaries, high-mass X-ray binaries (HMXBs), and hot, low-mass evolved stars (Flores-Fajardo et al. 2011). Features seen in the spectra of EIGs may include lines from helium (e.g., He II $\lambda1640$ and He II $\lambda4687$), nitrogen (e.g., N V $\lambda\lambda1240$, 1244), oxygen (e.g., O IV] $\lambda\lambda1401$, 1405), neon (e.g., [Ne IV] $\lambda2423$ and [Ne V] $\lambda\lambda3347$, 3427), iron (e.g., [Fe X] $\lambda6375$), and many others. These conditions appear indicative of rapidly accreting BHs or low-metallicity, recently formed stellar populations. We expect these conditions to be more apparent at higher redshifts, particularly in the EoR. Early work with the JWST suggests that many EoR galaxies have metallicities of ∼5%–10% $Z_\odot$ (e.g., Brinchmann 2023; Trump et al. 2023), and have also suggested the existence of active BH accretion in the very early Universe (e.g., Brinchmann 2023; Larson et al. 2023; Maiolino et al. 2023). In light of these recent results, it is prudent to consider the conditions that could produce EIGs at these early epochs.

In this work, we focus on emission from EIGs from quadruply ionized neon through [Ne V] $\lambda3427$[17] (vacuum wavelength) and its ratios with other bright UV/optical lines.

The ionization energy needed to produce Ne^{4+} (97.11 eV) is extremely high compared to most other strong UV/optical emission lines; [Ne V] emission requires energies nearly triple that of [O III] (35.12 eV), more than double that of [Ne III] (40.96 eV), and nearly double that of He II (54.42 eV). This property places [Ne V] well above the lower bound of the Berg et al. (2021) "very-high" ionization zone, and as such probes a parameter space of the ISM not traced by other strong UV/optical lines.[18]

The production of high-ionization emission lines such as [Ne V] requires an extremely hard photoionizing source. Previous works have attributed [Ne V] production to photoionization from AGNs, stellar continuum from an extremely hot ionizing spectrum including Wolf–Rayet stars, or energetic radiative shocks from supernovae (Gilli et al. 2010; Izotov et al. 2012; Mignoli et al. 2013; Zeimann et al. 2015; Backhaus et al. 2022; Cleri et al. 2023).

AGNs, produced from accretion onto BHs, are clear candidates for the production of photons needed to produce high-ionization emission lines.[19] Previous works have studied [Ne V] and its correlations with X-ray luminosities in local Seyferts and low-redshift ($z < 1.5$) quasi-stellar objects (QSOs; Gilli et al. 2010; Mignoli et al. 2013). Accretion onto intermediate-mass black holes (IMBHs) has remained an open field of study, though models predict that the accretion disks around IMBHs ($\log(M_{\mathrm{BH}}/M_\odot) \lesssim 5$) produce harder radiation fields than their supermassive counterparts (Done et al. 2012). These lower-mass accretion disk models are predicted to

---

[17] The near-UV/optical [Ne V] is a doublet with lines at 3427 Å and 3347 Å. However, the 3347 Å line is weaker (with a typical ratio of 2.73:1 for [Ne V] $\lambda3427$/[Ne V] $\lambda3347$) and the [Ne V] $\lambda3347$ line can be blended with other nearby lines (see Section 4.2 for more discussion). We therefore focus on [Ne V] $\lambda3427$ in this work.

[18] The $\gtrsim$100 eV energy regime also ionizes both hydrogen and helium to produce H I and He II photons; however, the minimum energy required to produce He II emission (54.42 eV) and HI emission (13.6 eV) is a factor of ∼2–7 lower than that of [Ne V] (97.11 eV).

[19] Here we use AGNs to indicate radiation from any accreting BH. This includes both AGNs associated with supermassive black holes (SMBHs; with $M_{\mathrm{BH}} \gtrsim 10^6\,M_\odot$) and AGNs arising from accretion onto more modest IMBHs with $M_{\mathrm{BH}} \lesssim 5\,M_\odot$, see, e.g., Cann et al. (2018).

emit photons hard enough to produce very-high-ionization (>54.42 eV) emission features (Cann et al. 2018).

Around the peak of cosmic star formation rate density and AGN activity at $z \sim 1-2$, studies have found that [Ne V] emission is consistent with photoionization from AGNs (Backhaus et al. 2022; Cleri et al. 2023). Cleri et al. (2023) finds that [Ne V]-emitting galaxies at these redshifts are five times more likely to be X-ray-confirmed AGNs than galaxies without [Ne V] detections, and that a majority (88%) of their objects are consistent with AGN emission in optical Baldwin et al. (1981; BPT)-like emission-line ratio diagnostics.

Some studies of local ($z \sim 0$) low-mass ($\log M_{*}/M_{\odot} \lesssim 8$), star-forming (SF) galaxies have explained [Ne V] production through energetic supernova shocks. Izotov et al. (2012) finds five oxygen-poor blue compact dwarf (BCD) galaxies with [Ne V] emission which have [Ne V]/He II flux ratios reproducible by radiative shock models with shock velocities in the 300–500 km s^{-1} range and shock ionizing contributions that are ~10% of that from the stellar continuum ionization. However, this modeling cannot conclusively rule out that this ~10% contribution of the [Ne V] emission comes from AGNs. These studies have primarily focused on low-mass galaxies (BCDs in the case of Izotov et al. 2012), so it is unclear if shocks can account for [Ne V] emission in more massive galaxies that dominate the peak of the cosmic star formation rate density. Alternatively, Olivier et al. (2022) has attributed local [Ne V] production to young (~5 Myr) extremely metal-poor ($Z \lesssim 0.1\, Z_{\odot}$) bursts of star formation plus an additional very hot ionizing source, modeled by an 80–100 kK blackbody (in excess of what is available in "normal" Population I or II stellar populations).

Another intriguing engine for the energetic photons required to produce [Ne V] is the exotic stellar populations in the very early Universe. Population III stars were likely very massive (>50 $M_{\odot}$; Zackrisson et al. 2011), with mass upper limits possibly even as great as 1000 $M_{\odot}$ (Bromm et al. 1999; Nakamura & Umemura 2002; Tan & McKee 2004; Greif & Bromm 2006; Ohkubo et al. 2009). Such chemically young populations likely initiated the metal enrichment of the succeeding generations of "normal" Population I and II stars in the later Universe (Heger et al. 2002). While truly primordial gas would not show metal emission, the chemical enrichment of the ISMs of early galaxies occurs rapidly given the short lifetimes of Population III stars (Finlator et al. 2015, 2016, 2018). However, the short lifetimes of these Population III stars introduce another complication; observation of high-ionization metal emission lines from the newly enriched ISM requires very recent ($\lesssim$1 Myr) star formation for such short-lived stars.

The spectral energy distributions (SEDs) of these Population III stars are most likely to peak in the extreme-UV (<912 Å), around the energies needed to ionize helium fully at 54.42 eV (Schaerer 2002; Zackrisson et al. 2011; Trussler et al. 2022). Stellar population synthesis codes predict that the SEDs of these Population III stars may produce photons at even higher energies, even into the very soft X-ray regime (see, e.g., the Yggdrasil models of Zackrisson et al. 2011; Trussler et al. 2022). This would allow for the production of ultrahigh-ionization emission lines like [Ne V] to be powered solely from these primordial stars provided the nebula ionized by these stars contains some elements heavier than He.

We can alleviate the potential degeneracies between Population III stars and other high-ionization sources (e.g., AGNs, supernova shocks, Wolf–Rayet stars, and HMXBs) with deeper information from rest-frame UV/optical spectra. The UV continuum can be used to derive the metallicity of the stellar populations, and the gas-phase metallicity can be derived from emission features. Other ionizing engines such as AGNs, supernova shocks, and Wolf–Rayet stars can produce broader emission features than standard H II regions, and X-ray observations can rule out HMXBs (e.g., Senchyna et al. 2020).

For objects which are not deeply observed across all wavelengths, separating photoionization from Population III stars and AGNs or other sources is often difficult (e.g., Katz et al. 2023a). Several works have offered potential solutions in the form of emission-line ratios of high-ionization to low-ionization lines (such as He II/Hβ), in conjunction with derived gas-phase metallicities (e.g., Schaerer 2002; Raiter et al. 2010; Inoue 2011; Katz et al. 2023a; Trussler et al. 2022).

In this work, we offer a potential diagnostic for photoionization from stellar populations or BH accretion disks using a combination of rest-frame UV/optical emission-line ratios ([O III]/Hβ, [Ne III]/[O II], and [Ne V]/[Ne III]). These line ratios are closely spaced in wavelength, and can be observed out to $z \sim 9$ in upcoming spectroscopic surveys of high redshifts with JWST.

The outline of this work is as follows. Section 2 describes our photoionization models. Section 3 describes our comparison samples. Section 4 compares the UV/optical emission-line ratios as diagnostics of AGN activity. Section 5 discusses the implications of our results. Section 6 summarizes the results of this work and discusses future studies of high-ionization galaxies with JWST.

2. Photoionization Models

To explore the physical conditions of EIGs throughout cosmic time, we employ photoionization modeling of local stellar populations, BH accretion disks, and Population III stars. For the following analysis, we use `Cloudy` version C17.01 (Ferland et al. 2017). `Cloudy` is a photoionization simulation code designed to model the physical conditions in astrophysical clouds self-consistently to predict the thermal, ionization, and chemical structure of the cloud and predict its observed spectrum.

Our models assume a hydrogen density of 10^2 cm^{-3}, with the `Cloudy` default Grevesse et al. (2010) solar abundance ratios and Orion dust grains for the initial gas phase and dust abundances. The emissivity of [Ne V]/[Ne III] is relatively insensitive to fluctuations in density (see Appendix B of Cleri et al. 2023). Unless otherwise stated, we assume a plane-parallel gas geometry for all models.

We run all of our models across a grid of ionization parameters[20] from $-4 < \log U < -1$ in steps of 0.25, where $U = q/c$ is the dimensionless ionization parameter. Kewley et al. (2019) defines the dimensionless ionization parameter as

$$U \equiv \frac{1}{c}\frac{\Phi}{n_{\mathrm{H}}}, \tag{1}$$

where Φ is the ionizing photon flux and n_{H} is the hydrogen density.

---

[20] This is the initial ionization parameter `Cloudy` assumes at the incident face of the cloud.

The details of the individual models used in this work are described in the following subsections.

2.1. "Normal" Stellar Population Models

The stellar population models used in this work are from the Binary Population and Spectral Synthesis (BPASS; v2.2.1) single-burst binary-formation library (Stanway & Eldridge 2018). The BPASS-only models use an initial mass function (IMF) with a Salpeter (1955) slope ($\alpha = -2.35$) for all masses, and an upper mass limit of 100 $M_\odot$. Unless otherwise stated, we use a single-burst stellar population with an age of 3 Myr, with stellar metallicities in a grid of $Z = 0.00005$, 0.05, 0.10, 0.20, 0.50, and 1.0 $Z_\odot$. We note that a $Z = 0.05\ Z_\odot$ gas-phase metallicity is consistent with extremely metal-poor dwarf galaxies ($Z < 0.1\ Z_\odot$) in the local Universe, and recent JWST spectra have not derived lower gas-phase metallicities than 5% solar (Berg et al. 2019, 2021; Brinchmann 2023; Olivier et al. 2022; Trump et al. 2023). We also use a composite stellar population model that adds to the BPASS models a hot (80 kK) blackbody needed to reproduce emission from very-high-ionization lines such as He II and C IV from Olivier et al. (2022; see Section 3.1).

2.2. "Exotic" Population III Star Models

To test exotic stellar populations potentially found in the early Universe, we also employ models of Population III stars from the Yggdrasil population synthesis code (Zackrisson et al. 2011). We use the Population III.1 model with a zero-metallicity population with an extremely top-heavy IMF (50–500 $M_\odot$) and a Salpeter (1955) slope ($\alpha = -2.35$) for all masses, with a single stellar population (SSP) from Schaerer (2002). We also use the Yggdrasil Population III.2 model, which is also a zero-metallicity stellar population but with a more moderately top-heavy IMF: log-normal with characteristic mass $M_c = 10\ M_\odot$, dispersion $\sigma = 1\ M_\odot$, extending from 1 to 500 $M_\odot$ (Tumlinson 2006; Raiter et al. 2010).

For these models, the stellar population is assumed to have zero metallicity, but we employ a (slightly) enriched gas-phase metallicity of $Z = 0.05\ Z_\odot$. For the very first population of stars, the gas-phase metallicity would be effectively null; this would yield no metal emission features, i.e., only hydrogen and helium emission. We assume that there must be some chemical enrichment in the ISM from primordial supernovae or stellar mass-loss events for metals to be present. This 5% solar gas-phase metallicity is consistent with extremely metal-poor dwarf galaxies in the local Universe, the most likely well-studied analogs to these high-redshift systems (e.g., Berg et al. 2016, 2019, 2021; Olivier et al. 2022).

2.3. Black Hole Accretion Models

Accretion onto BHs offers another source of high-energy photons that are capable of [Ne V] production. We tested both theoretical models for accretion onto BHs, as well as empirical models for AGNs.

The theoretical models for BH accretion are based on SEDs from Done et al. (2012). These models include a blackbody disk as well as a Compton upscattering component from the disk to recreate the "soft X-ray excess" often observed in AGNs in the local Universe (e.g., Walter & Fink 1993; Gierliński & Done 2004; Done et al. 2012). The final component to this model is a power-law tail used to model the high-energy emission which is the result of a second Compton upscattering that takes place in the optically thin corona above the disk. The Done et al. (2012) models are available in `XSPEC` (Arnaud 1996) using the OPTXAGNF command. We produce the SEDs of BHs with masses from 10^3 to $10^8 M_\odot$ and keep the parameters as the default parameters for this model except for the electron temperature associated with the soft Comptonization component, which we set to 0.1 keV instead of the default 0.2 keV as this is more similar to the models used by Cann et al. (2018).

Given the intricacies of accurately modeling BH accretion disk physics, the models used in this work are relatively simplistic (Adhikari et al. 2016; Mitchell et al. 2023). They employ a single cloud to represent the broad-line regions (BLRs) and NLRs, among other simplifications (Cann et al. 2018). More sophisticated models are an active area of work (e.g., J. Mckaig et al. 2023, in preparation). Potential improvements to these models include separate BLR and NLR physics, as well as other updates. These updated models are not likely to have a significant impact on the parameter space of interest in this work (i.e., $\lesssim$100 eV emission lines), but will include significant improvements at higher energies (J. Mckaig & S. Satyapal, private communication).

We derive the gas-phase metallicities for these BH accretion disk models from the mass–metallicity relation of Papovich et al. (2022). We derive the respective stellar masses for the galaxies surrounding these BH accretion disks using the Kormendy & Ho (2013) scaling relations. The Papovich et al. (2022) mass–metallicity relation is calibrated for more massive ($\gtrsim 10^9\ M_\odot$) ELGs around the peak of the cosmic star formation rate density and AGN activity at $z \sim 1-2$, so we extrapolate the relation for $M_{\rm BH} \leqslant 10^5\ M_\odot$, and set a minimum gas-phase metallicity for our lowest BH mass models of $Z = 0.05\ Z_\odot$.

To probe a representative of the AGN parameter space with a well-studied local active galaxy, we also include the SED of the nearby Seyfert 1 galaxy NGC 5548 (Mehdipour et al. 2015). NGC 5548 has a multiwavelength SED from near-infrared to hard (200 keV) X-rays. The UV to near-infrared continuum of NGC 5548 is consistent with being composed of a single Comptonized disk component, with no evidence of an additional purely thermal disk component or additional component of reprocessing from the disk. Notably, NGC 5548 also exhibits a "soft X-ray excess," which is correlated with the production of photons required to ionize neon to produce [Ne V]. NGC 5548 has a central engine powered by a $6.5 \times 10^7\ M_\odot$ SMBH (Bentz et al. 2007).

Several works suggest other empirical SED shapes for low-redshift Seyferts (Binette et al. 1989; Clavel et al. 1990) or high-redshift quasars (Korista et al. 1997; Zheng et al. 1997; Vanden Berk et al. 2001; Fan et al. 2006; Richards et al. 2006), yet these models are similar in shape to the Done et al. (2012) SEDs. Ultimately, the nature of AGN SEDs remains an open question, especially for the low-mass and low-luminosity regimes. Lower-mass accreting BHs ($\lesssim 10^5\ M_\odot$) may be key contributors to the high-ionization photon production of the early Universe, yet remain poorly understood.

2.4. Spectral Energy Distributions and `Cloudy` Output Spectra

Our photoionization models for BH accretion and stellar populations produce a wide range of emission at different energies. Figure 1 shows these input SEDs used in our

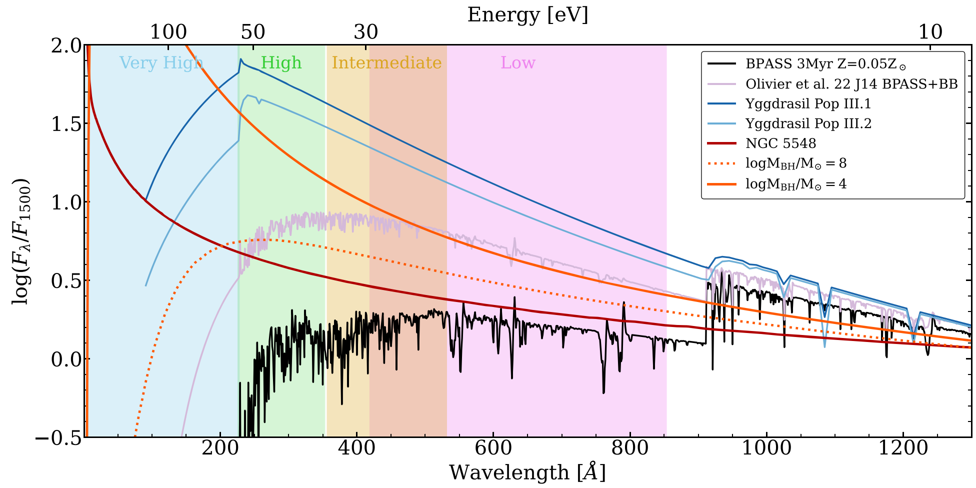

Figure 1. Example input SEDs of the various models used in our photoionization modeling. We show a pure BPASS 5% solar 3 Myr stellar population model in black, the Olivier et al. (2022) BPASS+blackbody model for J141851 in purple, the BH accretion disk models in orange ($\log M_{\rm BH}/M_\odot = 8$ dotted, $\log M_{\rm BH}/M_\odot = 4$ solid), NGC 5548 in red, and the Yggdrasil Population III.1 and III.2 models in dark and light blue, respectively. All models are normalized in F_λ at 1500 Å. The shaded regions mark the four zones of ionization from Berg et al. (2021; see Section 2).

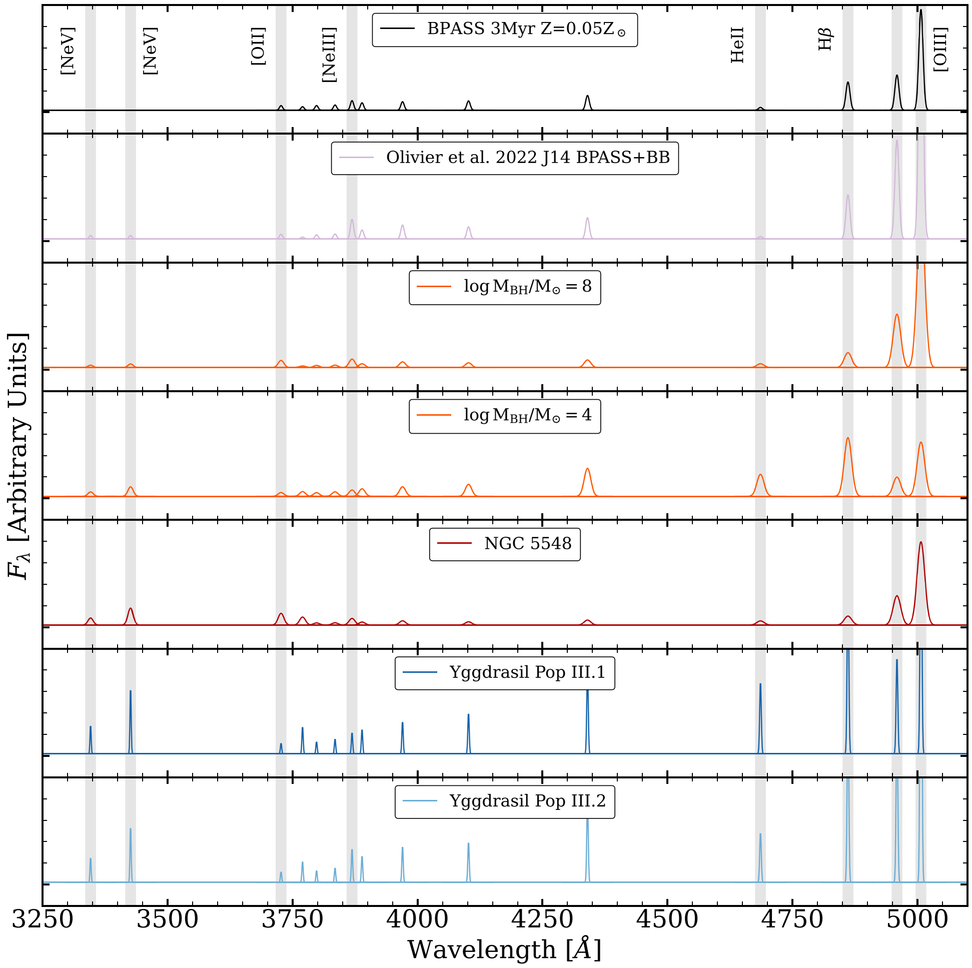

Figure 2. Example `Cloudy` output spectra of the various models used in this work. We show a pure BPASS 5% $Z_\odot$ 3 Myr stellar population model in black, the Olivier et al. (2022) BPASS+blackbody model for J141851 in purple, the BH accretion disk models in orange ($\log M_{\rm BH}/M_\odot = 8$ and $\log M_{\rm BH}/M_\odot = 4$), NGC 5548 in red, and the Yggdrasil Population III.1 and III.2 models in dark and light blue, respectively. We note several lines of interest: [Ne V] $\lambda\lambda$3347, 3427, [O II] $\lambda\lambda$3727, 3729, [Ne III] λ3870, He II λ4687, Hβ, and [O III] $\lambda\lambda$4960, 5008. For visualization purposes, we smooth the `Cloudy` spectra into Gaussians for each emission line (see Section 2 for details).

photoionization models. These include (i) a 3 Myr BPASS stellar population with continuum and gas-phase metallicity of 0.05 $Z_\odot$; (ii) a model that includes the 3 Myr BPASS stellar population with an additional 80 kK blackbody (needed to reproduce line ratios seen in the $z \sim 0$ metal-poor dwarf galaxy J141851; Olivier et al. 2022; see Section 3.1 for details); (iii) the Done et al. (2012) BH accretion disk models for BH masses ranging from $\log M_{\rm BH}/M_\odot = 4$ to $\log M_{\rm BH}/M_\odot = 8$; (iv) the Mehdipour et al. (2015) NGC 5548 SED; and (5) the Yggdrasil Population III.1 and III.2 SEDs. All of the models shown in Figure 1 are normalized at 1500 Å. We mark the four ionization zones of Berg et al. (2021):

1. Low ionization: energy needed to produce N^+ (14.53–29.60 eV).
2. Intermediate ionization: energy needed to produce S^{2+} (23.33-34.79 eV).
3. High ionization: energy needed to produce O^{2+} (35.11–54.93 eV).
4. Very high ionization: energy needed to produce He^{2+} (>54.42 eV).

Figure 2 shows the rest-frame NUV/optical `Cloudy` output intrinsic spectra from the respective ionizing SEDs in Figure 1. We mark several lines of interest: [Ne V] $\lambda\lambda$3347, 3427, [O II] $\lambda\lambda$3727, 3729, [Ne III] λ3870, He II λ4687, Hβ, and [O III] $\lambda\lambda$4960, 5008. We note that there is a large apparent difference between the spectra at the wavelengths of the [Ne V] lines. There is clear emission of [Ne V] in the AGN, NGC 5548, Population III.1, and Population III.2 spectra, but minimal [Ne V] in the BPASS 3 Myr or Olivier et al. (2022) BPASS +blackbody spectra. For visualization purposes, we smooth the `Cloudy` emission lines into Gaussians. We assume wind speeds of 250 km s^{-1} for the BPASS models and the Olivier et al. (2022) BPASS+blackbody models (see Olivier et al. 2022 for details), and 460 km s^{-1} for the BH accretion disk models and NGC 5548 (Peterson et al. 2013). For the Yggdrasil Population III models, we assume minimal 100 km s^{-1} winds; winds are metal driven, so true first-population stars will have zero wind (e.g., Baraffe & Kolb 2000; Kudritzki 2000; Schaerer 2002). The default spectral resolution of `Cloudy` is $R = 300$, so we note that there will be blending issues with other lines in the output spectra; as such, this Gaussian smoothing should be used only for visualization purposes.

3. Data

We compare our models to galaxies at $z \sim 0$ from Berg et al. (2021) and Olivier et al. (2022), $z \sim 1.6$ from Cleri et al. (2023), and $5 < z < 8.5$ from Trump et al. (2023), where for the latter we have made new measurements of [Ne V] as part of this work. We briefly describe these observations in the following subsections.

3.1. Observations at z ∼ 0

We compare our models with two galaxies in the nearby Universe which exhibit exceptional extreme emission-line behavior. These objects have been studied in detail in Berg et al. (2016, 2019, 2021) and Olivier et al. (2022):

1. J104457 has the largest C IV $\lambda\lambda$1548, 1550 equivalent width (−6.71 Å and −2.83 Å, respectively[21]) measured in the local Universe.
2. J141851 has the largest He II λ1640 equivalent width (−2.82 Å) measured in the local Universe.

J104457 and J141851 have far-UV spectra taken with the Cosmic Origins Spectrograph (COS) on the Hubble Space Telescope (HST; Proposal ID 15465) and near-UV/optical spectra from the Multi-Object Double Spectrograph (MODS) on the Large Binocular Telescope (LBT). They are both extremely metal-poor dwarf galaxies with derived gas-phase metallicities of 5.8% and 8.7% solar, respectively, and low stellar masses of $\log M_*/M_\odot = 6.80$ and 6.63, respectively.

3.1.1. Stellar Population+Blackbody Models

We also employ photoionization models used by Olivier et al. (2022) to reproduce the emission-line strengths of the two galaxies, J104457 and J141851. These models add (very hot) blackbodies to BPASS stellar populations in order to reproduce the emission of high-ionization spectral features such as C IV and He II. Olivier et al. (2022) matches the physical conditions of the galaxies (densities, abundances, etc.) and the full suite of low- to very-high-ionization lines in the rest-frame far-UV to optical to constrain the full shapes of the ionizing spectra. They find that the models which best reproduce the very-high-ionization emission in their galaxy J141851 (see Section 3.1) are those with stellar contributions from BPASS contributing 45% of the total luminosity, along with an injected 80 kK blackbody contributing the remaining 55% of the total luminosity (see the discussion in the next paragraph). These models use BPASS stellar populations with an IMF with a low-mass ($<0.5\ M_\odot$) slope of $\alpha = -1.3$, and high-mass ($>0.5\ M_\odot$) slope of $\alpha = -2.35$, with an upper mass limit of 100 $M_\odot$ (see Section 3 in Olivier et al. 2022).

Olivier et al. (2022) found that the ionizing spectra of J104457 and J141851 are consistent with extremely metal-poor stellar populations as represented by this extreme model that requires the addition of a hard photoionizing source, represented by the 80 kK blackbody, in order to produce the very-high-ionization lines. The physical origin of this hard photoionizing source is unknown, but could be the result of high-mass binaries, supersoft X-ray sources, stripped stars, or Wolf–Rayet stars, or a combination of these or other exotic populations (see Olivier et al. 2022 for a full discussion).

The two models for galaxies J104457 and J141851 take derived gas-phase metallicities of 5.8% and 8.7% solar, respectively. They assume a spherical cloud and scale nitrogen and carbon in the gas by their measured abundances (see Olivier et al. 2022 for more details).

3.2. Observations at z ∼ 1.6

The Cleri et al. (2023) sample of [Ne V]-emitting galaxies is selected from the CLEAR (Estrada-Carpenter et al. 2019, 2020; Simons et al. 2021, 2023) parent catalog of HST/Wide Field Camera 3 (WFC3) G102 and G141 grism observations using the following selection criteria:

1. Require a grism spectroscopic redshift, $1.39 < z < 2.30$, such that both [Ne V] and [O III] are within the observed-frame spectral range of G102 and G141 sensitivity (0.8–1.65 μm).
2. Require a signal-to-noise ratio (S/N) of at least 3 for [Ne V] λ3427 and [O III] $\lambda\lambda$4960, 5008.
3. Visual inspection of direct images with 1D and 2D spectra to ensure that no objects with poor continuum modeling and/or bad contamination subtraction make it into the final selection.

---

[21] Negative equivalent widths indicate emission features.

This selection leaves 25 galaxies with significant [Ne V] emission. See Cleri et al. (2023) for further details on the individual steps of the sample selection.

3.3. Observations at $5 < z < 8.5$

To test our models against galaxies in the EoR, we use the Trump et al. (2023) sample. This sample contains five galaxies at $5.2 < z < 8.5$ from JWST/NIRSpec observations of SMACS 0723 Early Release Observations (ERO; Pontoppidan et al. 2022). Each galaxy was observed with NIRSpec in two visits (s007 and s008; see Trump et al. 2023).

The Trump et al. (2023) results include measurements for several emission lines of interest: [O II] $\lambda\lambda$3727, 3729, [Ne III] λ3870, [O III] λ4364, Hγ, He II λ4687, Hβ, [O III] λ4960, and [O III] λ5008. In this work, we have refit the galaxies from the Trump et al. (2023) sample to probe for emission from [Ne V] λ3427. In three of the five sources we find possible detections of [Ne V] with S/N = 1–3. Of the two remaining galaxies, one shows no evidence of [Ne V] emission (S/N < 1). In the remaining galaxy, (ID 5144 in the catalog of Trump et al. 2023), the [Ne V] λ3427 line is not covered as its wavelength falls in a detector gap in the NIRSpec gratings. Figure 3 shows fits to the emission in the region of [Ne V] for the four galaxies with coverage. The detections of [Ne V] are marginal ($1 \lesssim$ S/N $\lesssim 3$) at best, but we include them as useful upper limits in our analysis below. We report the S/N ratios of the relevant emission lines as well as the [Ne V]/[Ne III] limits (see Section 4.2), [Ne III]/[O II], and [O III]/Hβ ratios and their uncertainties in Table 1. All of the values presented in Table 1 are for the coadded spectra between the two visits. [Ne V] λ3427 cannot be measured for ID 5144 as [Ne V] lies in a detector gap at this redshift. There is also a spectral artifact in the region of [Ne V] λ3427 in one visit of ID 8140.

4. Emission-line Ratio Classifications of Stellar Populations and Active Galactic Nuclei

4.1. The OHNO Diagram

The OHNO ([O III]/Hβ and [Ne III]/[O II]) diagram (Zeimann et al. 2015; Backhaus et al. 2022) is an emission-line ratio diagnostic designed to separate SF galaxies from AGNs around $z \sim 2$. This diagnostic compares the ratios of emission lines at similar wavelengths ([O II] $\lambda\lambda$3727, 3729, [Ne III] λ3870, Hβ, and [O III] $\lambda\lambda$4960, 5008) where the production of [O III] and [Ne III] both require higher photon energies: the first two ionization energies of oxygen (the minimum energies required to produce [O II] and [O III] photons) are 13.62 eV and 35.12 eV, respectively, and the second ionization energy of neon (the minimum energy required to produce [Ne III] photons) is 40.96 eV. Galaxies with strong [O III]/Hβ and/or [Ne III]/[O II] require harder radiation fields, typically found in the emission-line regions of AGNs. Backhaus et al. (2022) showed that division in the OHNO line ratios separates X-ray–selected AGNs from non-AGNs (based on classifications from the deep X-ray data in the Chandra Deep Fields at $z \sim 1$). Backhaus et al. (2022) defines the OHNO star formation/AGN dividing line as

$$\log\left(\frac{[\mathrm{O\,III}]}{\mathrm{H}\beta}\right) = \frac{0.35}{2.8\log([\mathrm{Ne\,III}]/[\mathrm{O\,II}]) - 0.8} + 0.64. \quad (2)$$

The OHNO diagnostic has also been used to show that [Ne V]-emitting galaxies near the peak of cosmic star formation and AGN activity at $z \sim 1-2$ are preferentially classified as AGNs (Backhaus et al. 2022; Cleri et al. 2023).

At high redshifts, it becomes difficult to distinguish between galaxies with photoionization from stellar populations and those with AGNs using only OHNO. We show the OHNO diagram in Figure 4. We also show our stellar, stellar +blackbody, and AGN models. We show our $z \sim 0$, $z \sim 1.6$, and $5 < z < 8.5$ comparison samples. We note that nearly all of the [Ne V]-emitting objects and the SMACS objects with [Ne V] limits are consistent with photoionization dominated by AGN activity by the Backhaus et al. (2022) diagnostic. For maximal completeness, we require an S/N greater than 1 for the OHNO emission lines. The BH accretion models and the NGC 5548 model show line ratios consistent with expectations for traditional AGNs with high-ionization parameters. We also show that extreme stellar populations are capable of producing line ratios which would be labeled as AGNs by the Backhaus et al. (2022) diagnostic.

4.2. The Ne53 Ratio

As [Ne V] requires ionization energies much higher than those of most other strong rest-frame UV/optical emission lines (97.11–125.26 eV), it probes extremely energetic photoionization missed by lower-energy tracers. By taking the ratio of [Ne V] to lower-ionization species, we can trace the physical conditions of the ISM missed by other line ratios, such as [O III]/Hβ, [Ne III]/[O II], [S II]/Hα, or [N II]/Hα. We define the Ne53 ratio as

$$\mathrm{Ne53} = \frac{\mathrm{Ne\ V}}{\mathrm{Ne\ III}\lambda3870}. \quad (3)$$

Ne53 is an opportunistic line ratio of study for several reasons. These species of neon evolve strongly with temperature and are relatively insensitive to changes in density (see Appendix A of Cleri et al. 2023), both [Ne V] and [Ne III] are accessible to JWST/NIRSpec spectroscopy from $z \sim 2$ to 12, and are close enough in wavelength for the ratio to be relatively insensitive to dust attenuation and instrumental effects such as calibration uncertainties. These two lines in particular also have the advantage of not being blended with other significant spectral features. For this reason, we choose to not use the [Ne v] λ3347, [Ne III] λ3968, or [Ne III] λ3343 lines in this ratio due to blending with each other or nearby lines at lower spectral resolutions.

The advantage of Ne53 is the large difference in minimum energy required to produce the emission lines: 97.11 eV for [Ne V] and 40.96 eV for [Ne III]. This traces the "very-high" to "high" ionization zones of Berg et al. (2021). Ne53 also has the advantage of eliminating any abundance degeneracy from using spectral lines of two different elements.

We explore Ne53 as an indicator of BH accretion or of the hard ionizing radiation from extreme stellar populations in Figure 5. We show a clear difference of several orders of magnitude between the AGN and BPASS/BPASS+blackbody models in Ne53 space; especially interesting is that the Population III star models are competitive with AGNs in the production of [Ne V] relative to [Ne III], with the Population III models residing in a similar region of the parameter space as the low-mass ($M_{\mathrm{BH}} \leqslant 10^5\ M_\odot$) BH accretion disk models. The BPASS-only models fail to produce any meaningful [Ne V], with log(Ne53) ratios peaking around -5 for all metallicities.

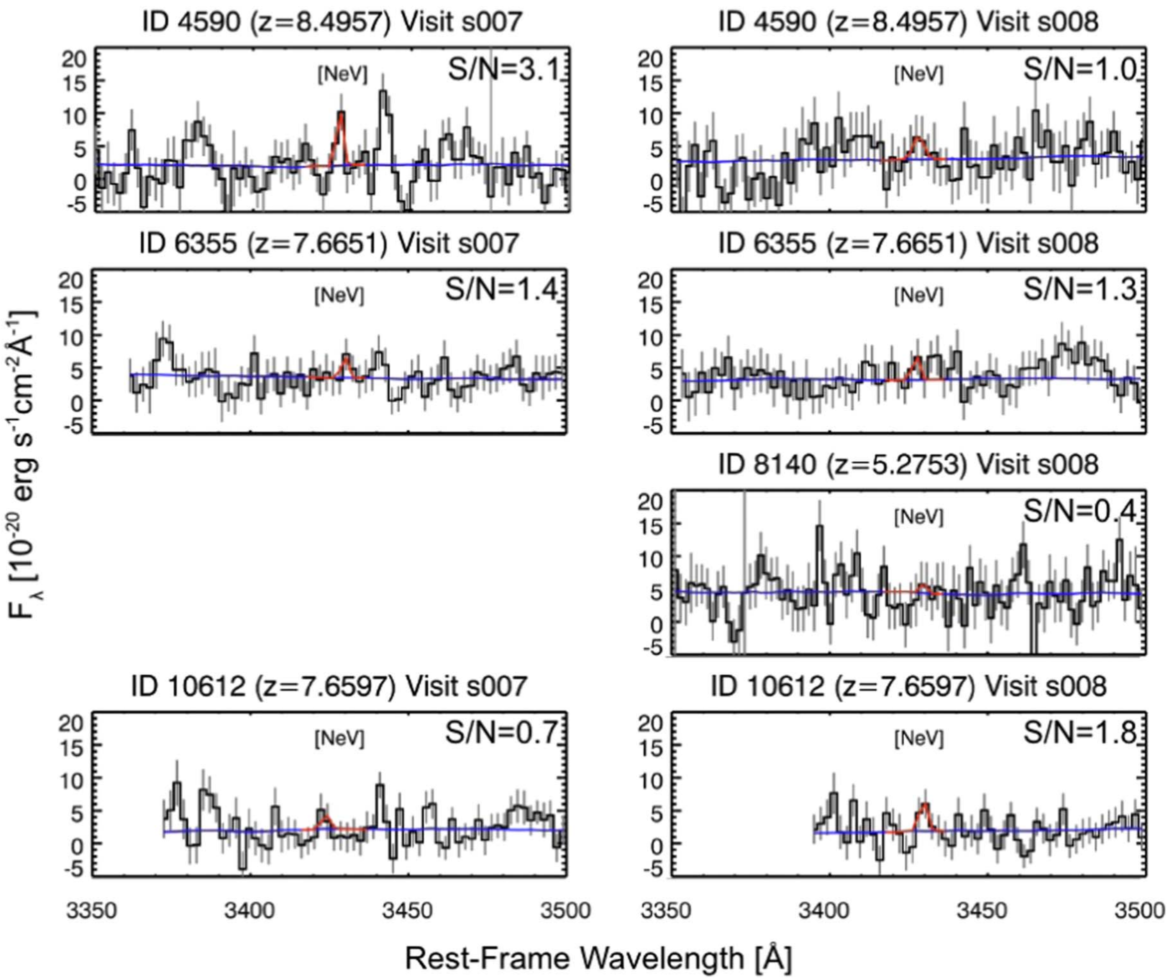

Figure 3. Fits to [Ne V] $\lambda 3427$ for the four $5.3 < z < 8.5$ SMACS ERO galaxies from the Trump et al. (2023) sample with [Ne V] coverage in JWST/NIRSpec. Each row shows the spectra for one object (with IDs from Trump et al. 2023 labeled) where the two panels in each row show the spectra from the two different visits ("'s007" and "s008," respectively). The blue and red lines denote the continuum and emission-line fits, respectively. We show the S/N for the fit in each visit. We do not show the first visit for ID 8140 as there is a spectral artifact at the observed wavelength of [Ne V] $\lambda 3427$, making an accurate line measurement impossible. We note that none of these objects are well detected (S/N > 3) in [Ne V] by coadding spectra between visits. The S/Ns and relevant emission-line ratios for these objects are given in Table 1.

We include polygons in Figure 5 to mark the general locations of different ionizing engines in this parameter space. We empirically separate the [O III]/Hβ versus Ne53 diagram into four regions:

1. log(Ne53) < -5: objects dominated by "normal" star formation alone.
2. log([O III]/Hβ) < 1 and $-5 <$ log(Ne53) < -0.3: "composite" zone of multiple potential ionizing sources.
3. (log([O III]/Hβ) > 1 and $-5 <$ log(Ne53) < -0.3) or (log([O III]/Hβ) > 0.6 and log(Ne53) > -0.3): "traditional" SMBH accretion disk AGNs.
4. log([O III]/Hβ) < 0.6 and log(Ne53) > -0.3: Population III stars or IMBH accretion disks.

We show our photoionization models compared to our $z \sim 0$, $z \sim 1.6$, and $5 < z < 8.5$ samples to show that objects with well-detected [Ne V] emission are many orders of magnitude inconsistent with stellar population–only models from BPASS, even at the highest ionization parameters. We also show that the 3σ upper limits of Ne53 place the SMACS galaxies at $5 < z < 8.5$ near the boundary of the composite and AGN/Population III/IMBH regions, but we do not draw any significant conclusions due to the low S/Ns of these measurements.

5. Discussion

The emission-line ratio diagnostics of Figures 4 and 5 carry many implications of the nature of EIGs and [Ne V] emission. The Ne53 ratio (see Figure 5) separates AGN and Population III models from BPASS/BPASS+blackbody stellar models by several orders of magnitude at a given ionization parameter. As such, we conclude that the Ne53 ratio is an effective diagnostic of hard radiation fields. However, there is a large region where the Ne53 and [O III]/Hβ ratios could stem from star formation or AGNs (labeled "composite" in Figure 5), but any object that resides in this region is of interest as they will be EIGs with possible indications of exotic stellar populations, accreting IMBHs, or both. Therefore, Ne53 alone is not sufficient to separate AGNs from extreme stellar populations, such as those presented in our Population III models.

The OHNO diagnostic (Figure 4) shows that nearly all of the compared galaxies with [Ne V] detections (or upper limits to [Ne V] for the SMACS objects) are consistent with photoionization from an AGN, as defined by the Backhaus et al. (2022)

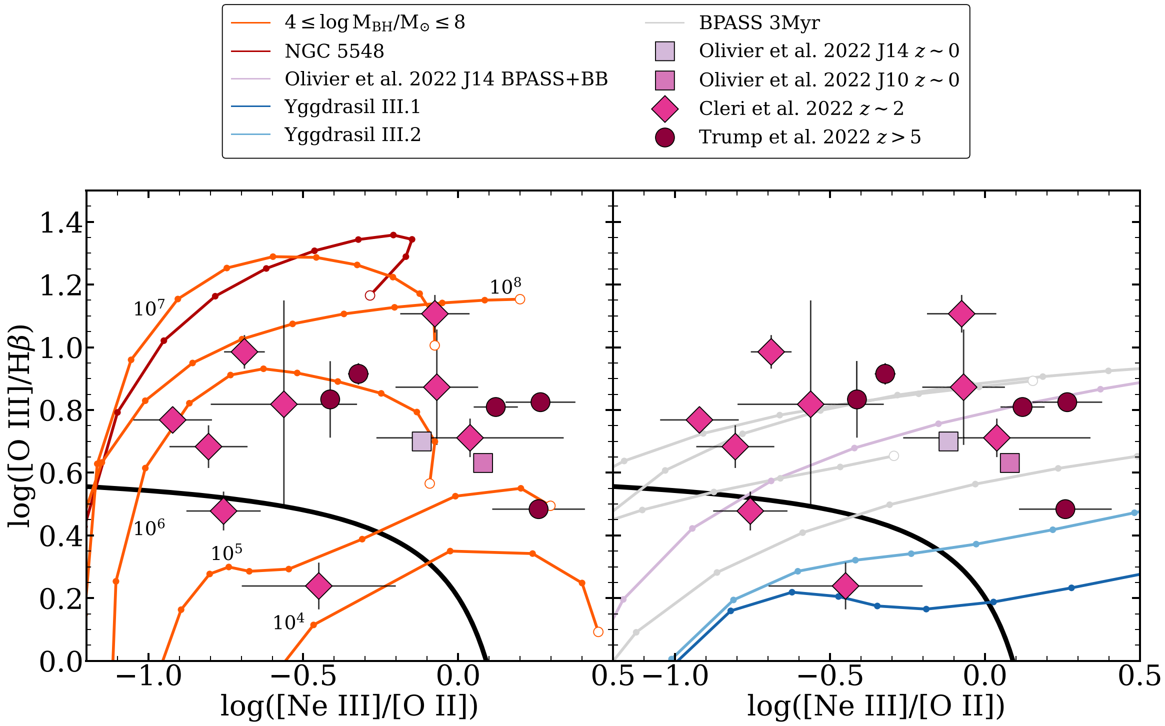

Figure 4. The OHNO diagram of log([O III]/Hβ) vs. log([Ne III]/[O II]). Models are shown in a grid of dimensionless ionization parameter $-4 \leqslant \log U \leqslant -1$, with the open symbol at the end of each track marking $\log U = -1$. Left: AGN models in OHNO parameter space. We also show the NGC 5548 SED from Mehdipour et al. (2015) in red, and BH accretion disk models from $4 \leqslant \log M_{BH}/M_\odot \leqslant 8$ in orange, with annotations indicating the BH mass of each model. Right: stellar population models in OHNO parameter space. We show the BPASS 3 Myr stellar populations of a range of metallicities, $Z = 0.00005$, 0.05, 0.10, 0.20, 0.50, and 1 $Z_\odot$, in gray. We also include the Olivier et al. (2022) BPASS+blackbody model for J141851 in purple, and the Yggdrasil Population III.1 and III.2 models in dark and light blue, respectively. In each panel we show the $z \sim 0$ data from Olivier et al. (2022), $z \sim 2$ observations from Cleri et al. (2023), and $z > 5$ observations from Trump et al. (2023).

Table 1
Measurements from NIRSpec Data of SMACS Galaxies

ID	Redshift	[Ne V] λ3427[a]	[O II] $\lambda\lambda$3727, 3729[a]	[Ne III] λ3870[a]	Hβ[a]	[O III] λ5008[a]	[Ne V]/ [Ne III][b]	[Ne III]/[O II]	[O III] λ5008/Hβ
4590	8.4957	2.3	3.2	6.8	20.4	38.3	<0.61	1.82 ± 0.63	3.05 ± 0.17
5144	6.3792	...	7.4	10.8	27.4	86.3	...	1.32 ± 0.22	6.45 ± 0.25
6355	7.6651	1.8	23.5	15.5	26.3	96.5	<0.20	0.48 ± 0.04	8.23 ± 0.32
8140	5.2753	0.4	13.7	4.6	6.9	28.6	<0.44	0.39 ± 0.09	6.82 ± 0.98
10612	7.6597	1.8	4.2	13.0	23.6	77.5	<0.36	1.84 ± 0.48	6.97 ± 0.31

Notes.
[a] S/N ratio of the respective emission line.
[b] 3σ upper limit for [Ne V] λ3427 nondetection.

division (Equation (2)). This result shows that the OHNO diagram is not an accurate diagnostic for the most extreme emission-line galaxies in the local Universe, given our comparison to J141851 and J104457 from Olivier et al. (2022) and Berg et al. (2019, 2021). This is likely due to the calibration of the OHNO AGN/SF division from Backhaus et al. (2022) being based on much higher mass X-ray AGNs at $z \sim 1 - 2$, and as such OHNO is not designed to discriminate AGN emission from low-mass metal-poor EIGs like J104457 and J141851.

If very-high-redshift galaxies are similar to the EIGs studied by Olivier et al. (2022), then the Backhaus et al. (2022) OHNO division between AGNs and SF galaxies may be inaccurate. As such, we do not adhere to the OHNO classifications of the SMACS ERO objects at $z > 5$ as AGNs. Other works have conjectured that a subset of these objects may be narrow-line AGNs (Brinchmann 2023), but there is not conclusive evidence from other metrics for the AGN nature of any of these galaxies.

Our BH accretion disk models for AGNs cover a wide region of the OHNO parameter space. The higher BH mass ($M_{BH} \geqslant 10^6\ M_\odot$) models produce higher [O III]/Hβ and lower [Ne III]/[O II] ratios than the lower BH mass models. The higher BH mass models are similar to the galaxies in the $z \sim 2$ comparison sample of [Ne V] emitting galaxies from Cleri et al. (2023), which is most similar to the Backhaus et al. (2022) sample from which the OHNO diagnostic was derived.

The photoionization models show increased [Ne III]/[O II] compared to [O III]/Hβ for AGNs, along with increased [O III]/Hβ from the BPASS+blackbody models from Olivier et al. (2022). As a useful proof of concept for the variable M_{BH} accretion disk models, we note that the NGC 5548 model

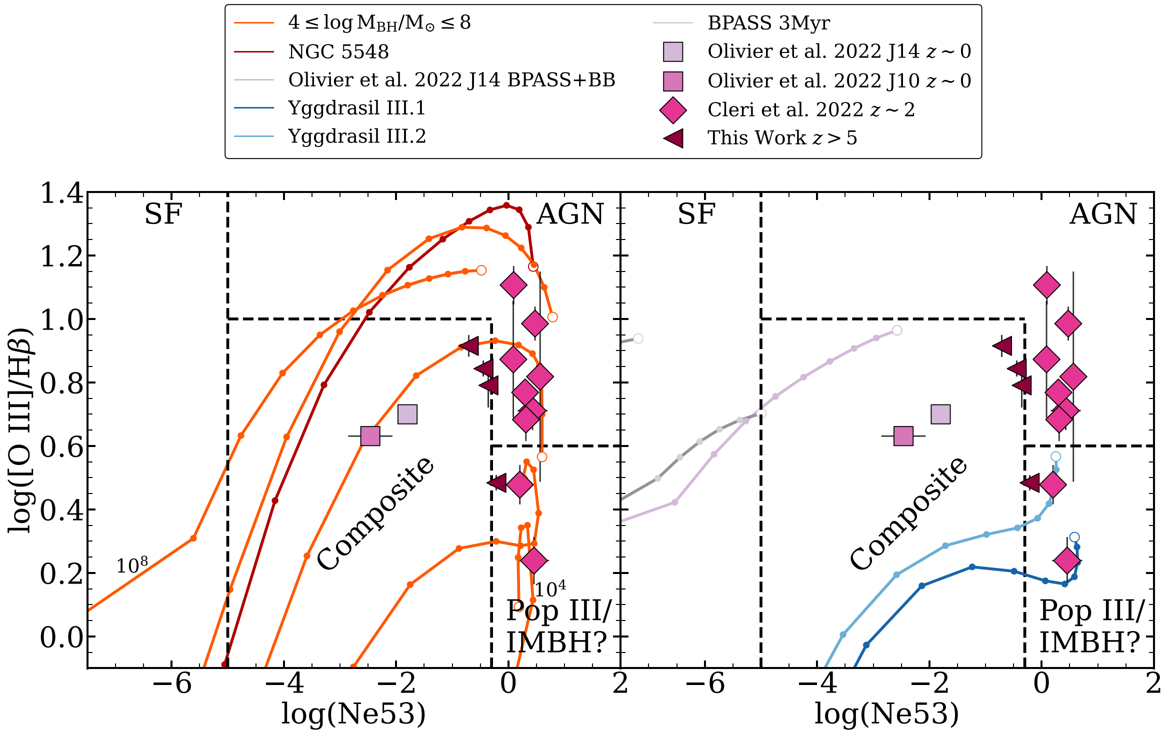

Figure 5. The relation between the [O III]/Hβ and [Ne V]/[Ne III] (Ne53) ratios. Models are shown in a grid of dimensionless ionization parameter $-4 \leqslant \log U \leqslant -1$, with the open symbol at the end of each track marking $\log U = -1$. Left: log([O III]/Hβ) vs. log(Ne53) showing AGN models. We show the variable $M_{\rm BH}$ accretion disk models in orange, marking the extremes of $\log M_{\rm BH}/M_{\odot} = 8$ and $\log M_{\rm BH}/M_{\odot} = 4$, and the NGC 5548 SED from Mehdipour et al. (2015) in red. Right: log([O III]/Hβ) vs. log(Ne53) showing stellar population models. We show the BPASS 3 Myr stellar population models in gray for metallicities $Z = 0.00005$, 0.05, 0.10, 0.20, 0.50, and 1 $Z_{\odot}$ (most lines are off the plot left). We also include the Olivier et al. (2022) BPASS+blackbody model for the local high-ionization metal-poor dwarf J141851 in purple, and the Yggdrasil Population III.1 and III.2 models in dark and light blue, respectively. In each panel we show the $z \sim 0$ data from Olivier et al. (2022), $z \sim 2$ observations from Cleri et al. (2023), and $z > 5$ observations from Trump et al. (2023) including their 3σ upper limits on Ne53 as measured in this work. We note a distinct separation between the parameter space covered by the AGN models and the BPASS stellar populations. The BPASS models are unable to reproduce the observed Ne53 ratios, even at the highest ionization parameters. The dashed black lines delineate regions where the line ratios are mostly consistent with ionization from star formation (SF), AGNs, a composite of potential SF and AGNs, and possible ionization from Population III stars or accretion onto IMBHs.

resides in a similar parameter space as the high-mass ($M_{\rm BH} \geqslant 10^7\ M_{\odot}$) Done et al. (2012) models. We also note that the Population III models occupy the lowest [O III]/Hβ but highest [Ne III]/[O II] ratios of any of the models presented.

Other non-AGN and non-SF explanations of [Ne V] emission remain an open question. Other works have attributed [Ne V] emission in small samples of galaxies to shocks from supernovae (Izotov et al. 2012, 2021; Leung et al. 2021), but are unable to rule out production via AGNs on the population level.

Perhaps the most intriguing alternative explanation for [Ne V] production in the early Universe is through exotic Population III stars. While exact constraints on the nature of Population III stars and the high-redshift IMF remain unknown, we show that current models of Population III stars are indeed capable of providing the energetic radiation necessary to produce ultrahigh-ionization emission features such as [Ne V] (see Figure 5).

Throughout the analyses performed in this work, we have identified an interesting diagnostic for Population III stars and IMBH accretion disks. The emission-line ratio relations in Figures 4 and 5 can be used in conjunction to separate objects into four distinct groups (see Section 4 for exact delineations):

1. Objects dominated by star formation do not produce significant [Ne V], thus lie very low (or undetectable) in Ne53 (Figure 5).
2. AGNs dominated by SMBH ($M_{\rm BH} \geqslant 10^6\ M_{\odot}$) accretion disks produce high [O III]/Hβ ratios, consistent with traditional star formation/AGN diagnostics (e.g., Baldwin et al. 1981; Veilleux & Osterbrock 1987; Backhaus et al. 2022).
3. Objects dominated by Population III stars or AGNs with lower-mass BHs (IMBHs, with $M_{\rm BH} \lesssim 10^5\ M_{\odot}$) reside in a unique parameter space in the emission-line ratio relations in this work. These objects are low in [O III]/Hβ, yet high in both [Ne III]/[O II] and Ne53, similar to the parameter space occupied by the Population III models.
4. A composite region for objects which have spectra with contributions from a variety of ionizing sources.

Objects with significant contributions to their spectra from Population III stars and lower-mass BH accretion disks are poorly understood. Information from emission-line ratios such as those presented in this work will offer insight into the physical conditions of these interesting objects.

We look to future observations from the JWST and next-generation facilities to offer constraints on these exotic stellar populations through emission-line spectroscopy of EIGs. Recent studies (Trussler et al. 2022) have suggested that JWST is capable of detecting $M_{*} = 10^6\ M_{\odot}$ Population III galaxies at $z \sim 8$ spectroscopically, with (very) deep integrations of tens to hundreds of hours of NIRSpec/G140M time. However, Trussler et al. (2022) calculates that moderately lensed or more massive ($M_* = 2-3 \times 10^6\,M_\odot$) Population III galaxies will be detectable with medium-sized JWST General Observer programs (25–75 hr).

We caution against the general use of lower-ionization emission-line ratio diagnostics of star formation and AGNs (e.g., BPT, VO87, OHNO, etc.) for high-redshift systems as the sole discriminator between sources of ionization. In general, the use of emission-line ratio diagnostics for objects or redshift regimes for which they are not designed is questionable. Recent works have discussed the need for more emission-line ratio diagnostics which are more robust across redshifts, e.g., Figure 5 in this work. Instead, we suggest the aggregation of multiple tracers of BH accretion/extreme stellar populations to make decisive conclusions about the nature of the ionizing spectra of high-redshift objects: emission-line velocity profiles, broad-line components, multiwavelength luminosities (X-ray, radio, mid-IR, etc.), and so on (see Larson et al. 2023 for a discussion of AGN tracers for the current highest-redshift AGN candidate at $z = 8.7$).

6. Summary and Conclusions

In this work, we used photoionization models to explore the physical conditions of [Ne V] λ3427 emission in EIGs across cosmic time. We produce `Cloudy` photoionization models using incident SEDs from BPASS stellar populations alone (Stanway & Eldridge 2018), variable-mass BH accretion disks (Done et al. 2012; Cann et al. 2018), the well-studied local Seyfert NGC 5548 (Mehdipour et al. 2015), and the Yggdrasil Population III.1 and III.2 models (Zackrisson et al. 2011). We also include the BPASS stellar populations plus an 80 kK blackbody model of local metal-poor dwarf galaxy J141851 (Olivier et al. 2022). We compare our results to observations of galaxies at $z \sim 0$ (Berg et al. 2016, 2019, 2021; Olivier et al. 2022), $z \sim 2$ (Cleri et al. 2023), and $5 > z > 8.55$ (Trump et al. 2023).

The primary findings of this work are as follows:

1. We fit for [Ne V] in the $z > 5$ SMACS 0723 sample from Trump et al. (2023), and find no significant (S/N > 3) detections in the four objects for which there is JWST/NIRSpec coverage of [Ne V]. We find marginal (1 < S/N < 3) detections for three objects (one object with S/N < 1), which we use to assess the limiting behavior in our emission-line ratio diagnostics. We publish our measured [Ne V] λ3427 S/N ratios and emission-line ratios in Table 1.
2. The [Ne V]/[Ne III] (Ne53) ratio is an effective indicator of photoionization from a source other than "normal" stellar populations. Current photoionization models cannot reproduce [Ne V] emission with "normal" stellar populations alone (such as those from the BPASS models, see Figure 5). We conclude that the measurement of any meaningful detection of Ne53 (log(Ne53) $\gtrsim -5$) likely implies the presence of an ionizing engine other than "normal" stellar populations alone (e.g., likely either AGNs or Population III stars).
3. We use Ne53 in conjunction with other line ratios to produce a diagnostic of AGN and Population III star activity. We propose the combination of Figures 5 and 4 to be used as such a diagnostic, where we anticipate galaxies with significant contributions of their ionizing radiation from Population III stars or low-mass AGNs ($M_{\rm BH} \leqslant 10^5\,M_\odot$) to reside in low [O III]/Hβ (log([O III]/Hβ) $\lesssim 0.6$) and high [Ne III]/[O II] (log([Ne III]/[O II]) $\gtrsim 0$) and Ne53 (log(Ne53) $\gtrsim$ –0.3, indicating very-high ionization) parameter spaces. We propose that Figure 5 can be used in future studies in conjunction with other AGN tracers (e.g., velocity profiles, broad-line components, X-ray/radio/mid-IR luminosities, etc.) to separate sources of ionizing radiation further.

Our results show that [Ne V] emission probes highly energetic photoionization ($\sim$100 eV), which, for the models used in this work, is only reproducible by BH accretion or Population III stars. Although we attribute the [Ne V] production in many of the galaxies in our comparison samples, we also note that there are other production mechanisms, namely supernova shocks or other exotic stellar populations (e.g., Wolf–Rayet stars). We note that the unknown nature of Population III stars and low-mass BH accretion disks in the early Universe indicates that EoR galaxies are an exciting laboratory in which to study these extreme emission lines. We also note that the potential coevolution of accreting BHs and stellar populations in the early Universe can have competing contributions to the production of high-ionization emission lines. Regardless, galaxies that show strong Ne53 and low [O III]/Hβ will be candidates for rare sources and may guide us to galaxies with ionization from either the first stars or AGNs with lower-mass BHs.

As such, these results motivate future observations of very-high-ionization emission lines, like [Ne v] λ3427, using cutting-edge observatories like the JWST. JWST will reach a flux limit that is an order of magnitude fainter than the HST data from the Cleri et al. (2023) sample for similar exposure times, enabling detection of fainter [Ne V] line emission. JWST is outfitted with NIRSpec and NIRCam, both of which have spectroscopic capabilities covering strong UV high-ionization emission lines, like the [Ne V] doublet, over a range of redshift (e.g., $6 < z < 11$). Even JWST/NIRISS can cover [Ne V] at slightly lower redshift ranges ($3 < z < 7$).

JWST/MIRI even provides low- ($R \sim 100$) and medium-resolution ($R \sim 1500$–3500) spectroscopy, which covers 5–28 μm. This will allow observations of rest-frame UV/optical spectral features for bright galaxies out to ultrahigh-redshifts ($z > 15$). Spectroscopy in this very early epoch in cosmic history will give direct measurements of first-generation stellar populations, as well as the beginning of chemical enrichment of the ISM.

The potential degeneracy of [Ne V] production from low-mass BH accretion disks or Population III stars in the early Universe is difficult to break with rest-frame UV/optical line ratios alone. In addition to the integrated emission-line diagnostics we present in this work (Figures 4 and 5), we can pose a solution using the integral field unit capabilities of JWST/NIRSpec by looking at the spatial distribution and compactness of the high-ionization emission. We expect galaxies with significant Population III fractions to be more uniformly distributed in their [Ne V] emission (or other very-high-ionization emission) than an AGN, where we expect the emission to be highly centrally dense. We can also break this degeneracy with more spectral information, including more detailed chemical abundances and metallicities.

Future studies using current and next-generation systems of high-redshift systems through the lens of extreme high-ionization emission lines, including [Ne V], will offer long-awaited answers to the underlying physics of the EoR.

Acknowledgments

This work is based on data obtained from the Hubble Space Telescope through program number GO-14227. Support for Program number GO-14227 was provided by NASA through a grant from the Space Telescope Science Institute, which is operated by the Association of Universities for Research in Astronomy, Incorporated, under NASA contract NAS5-26555. N.J.C., J.R.T., and B.E.B. acknowledge support from NSF grant No. CAREER-1945546 and NASA grant Nos. JWST-ERS-01345 and 18-2ADAP18-0177. N.J.C., J.R.T., C.P., and B.E.B. acknowledge support from NASA grant No. JWST-ERS-01345. N.J.C. and C.P. also acknowledge support from NASA/HST AR 16609. This work acknowledges support from the NASA/ESA/CSA James Webb Space Telescope through the Space Telescope Science Institute, which is operated by the Association of Universities for Research in Astronomy, Incorporated, under NASA contract NAS5-03127. Support for program No. JWST-ERS01345 was provided through a grant from the STScI under NASA contract NAS5-03127. T.A.H. and A.Y. are supported by appointments to the NASA Postdoctoral Program (NPP) at NASA Goddard Space Flight Center, administered by Oak Ridge Associated Universities under contract with NASA.

The authors thank Shobita Satyapal, Jeffrey Mckaig, and Jenna Cann for discussion and providing assistance with photoionization modeling. N.J.C. thanks Jonathan Cohn, Justin Cole, and Maeve Curliss for insightful scientific and data visualization discussions. N.J.C. also thanks the CANDELS Lyα Emission at Reionization (CLEAR) and Cosmic Evolution Early Release Science (CEERS) collaborations for influential discussions.

Some of the data presented in this paper were obtained from the Mikulski Archive for Space Telescopes (MAST) at the Space Telescope Science Institute. The Berg et al. (2019) and Olivier et al. (2022) data are from HST Project ID 15465. The SMACS 0723 data from Simons et al. (2023) can be accessed via doi:10.17909/t9-ctff-wx60 while the SMACS 0723 data from Trump et al. (2023) can be accessed via doi:10.17909/67ft-nb86.

Software: `grizli` (Brammer et al. 2008), FAST (Kriek et al. 2009), EAZY (Brammer et al. 2008; Wuyts et al. 2011), Astropy (Astropy Collaboration et al. 2013), NumPy (Harris et al. 2020), Matplotlib (Hunter 2007), `Cloudy` (Ferland et al. 2017), seaborn (Waskom 2021), pandas (Reback et al. 2022), and `XSPEC` (Arnaud 1996).

ORCID iDs

Nikko J. Cleri https://orcid.org/0000-0001-7151-009X
Grace M. Olivier https://orcid.org/0000-0002-4606-4240
Taylor A. Hutchison https://orcid.org/0000-0001-6251-4988
Casey Papovich https://orcid.org/0000-0001-7503-8482
Jonathan R. Trump https://orcid.org/0000-0002-1410-0470
Ricardo O. Amorín https://orcid.org/0000-0001-5758-1000
Bren E. Backhaus https://orcid.org/0000-0001-8534-7502
Danielle A. Berg https://orcid.org/0000-0002-4153-053X
Vital Fernández https://orcid.org/0000-0003-0531-5450
Steven L. Finkelstein https://orcid.org/0000-0001-8519-1130
Seiji Fujimoto https://orcid.org/0000-0001-7201-5066
Michaela Hirschmann https://orcid.org/0000-0002-3301-3321
Jeyhan S. Kartaltepe https://orcid.org/0000-0001-9187-3605
Dale D. Kocevski https://orcid.org/0000-0002-8360-3880
Raymond C. Simons https://orcid.org/0000-0002-6386-7299
Stephen M. Wilkins https://orcid.org/0000-0003-3903-6935
L. Y. Aaron Yung https://orcid.org/0000-0003-3466-035X

References

Adhikari, T. P., Różańska, A., Czerny, B., Hryniewicz, K., & Ferland, G. J. 2016, ApJ, 831, 68
Amorín, R., Fontana, A., Pérez-Montero, E., et al. 2017, NatAs, 1, 0052
Amorín, R., Pérez-Montero, E., Contini, T., et al. 2015, A&A, 578, A105
Arnaud, K. A. 1996, in ASP Conf. Ser. 101, Astronomical Data Analysis Software and Systems V, ed. G. H. Jacoby & J. Barnes (San Francisco, CA: ASP), 17
Astropy Collaboration, Robitaille, T. P., Tollerud, E. J., et al. 2013, A&A, 558, A33
Atek, H., Siana, B., Scarlata, C., et al. 2011, ApJ, 743, 121
Backhaus, B. E., Trump, J. R., Cleri, N. J., et al. 2022, ApJ, 926, 161
Baldwin, J. A., Phillips, M. M., & Terlevich, R. 1981, PASP, 93, 5
Baraffe, I., & Kolb, U. 2000, MNRAS, 318, 354
Bentz, M. C., Denney, K. D., Cackett, E. M., et al. 2007, ApJ, 662, 205
Berg, D. A., Chisholm, J., Erb, D. K., et al. 2019, ApJL, 878, L3
Berg, D. A., Chisholm, J., Erb, D. K., et al. 2021, ApJ, 922, 170
Berg, D. A., Skillman, E. D., Henry, R. B. C., Erb, D. K., & Carigi, L. 2016, ApJ, 827, 126
Binette, L., Prieto, A., Szuszkiewicz, E., & Zheng, W. 1989, ApJ, 343, 135
Brammer, G. B., van Dokkum, P. G., & Coppi, P. 2008, ApJ, 686, 1503
Brinchmann, J. 2023, MNRAS, in press
Bromm, V., Coppi, P. S., & Larson, R. B. 1999, ApJL, 527, L5
Buat, V., Boselli, A., Gavazzi, G., & Bonfanti, C. 2002, A&A, 383, 801
Cann, J. M., Satyapal, S., Abel, N. P., et al. 2018, ApJ, 861, 142
Clavel, J., Boksenberg, A., Bromage, G. E., et al. 1990, MNRAS, 246, 668
Cleri, N. J., Yang, G., Papovich, C., et al. 2023, ApJ, 948, 112
Curtis-Lake, E., Carniani, S., Cameron, A., et al. 2023, NatAs, 7, 622
Done, C., Davis, S. W., Jin, C., Blaes, O., & Ward, M. 2012, MNRAS, 420, 1848
Dopita, M. A., Kewley, L. J., Heisler, C. A., & Sutherland, R. S. 2000, ApJ, 542, 224
Estrada-Carpenter, V., Papovich, C., Momcheva, I., et al. 2019, ApJ, 870, 133
Estrada-Carpenter, V., Papovich, C., Momcheva, I., et al. 2020, ApJ, 898, 171
Fan, X., Strauss, M. A., Becker, R. H., et al. 2006, AJ, 132, 117
Ferland, G. J., Chatzikos, M., Guzmán, F., et al. 2017, RMxAA, 53, 385
Finkelstein, S. L., Ryan, R. E. J., Papovich, C., et al. 2015, ApJ, 810, 71
Finlator, K., Keating, L., Oppenheimer, B. D., Davé, R., & Zackrisson, E. 2018, MNRAS, 480, 2628
Finlator, K., Oppenheimer, B. D., Davé, R., et al. 2016, MNRAS, 459, 2299
Finlator, K., Thompson, R., Huang, S., et al. 2015, MNRAS, 447, 2526
Flores-Fajardo, N., Morisset, C., Stasińska, G., & Binette, L. 2011, MNRAS, 415, 2182
Gierliński, M., & Done, C. 2004, MNRAS Lett., 349, L7
Gilli, R., Vignali, C., Mignoli, M., et al. 2010, A&A, 519, A92
Greif, T. H., & Bromm, V. 2006, MNRAS, 373, 128
Grevesse, N., Asplund, M., Sauval, A. J., & Scott, P. 2010, Ap&SS, 328, 179
Groves, B., Brinchmann, J., & Walcher, C. J. 2012, MNRAS, 419, 1402
Harris, C. R., Millman, K. J., van der Walt, S. J., et al. 2020, Natur, 585, 357
Heger, A., Woosley, S., Baraffe, I., & Abel, T. 2002, in Lighthouses of the Universe: The Most Luminous Celestial Objects and Their Use for Cosmology, ed. M. Gilfanov, R. Sunyeav, & E. Churazov (Garching: Springer-Verlag), 369
Hunter, J. D. 2007, CSE, 9, 90
Inoue, A. K. 2011, MNRAS, 415, 2920
Izotov, Y. I., Thuan, T. X., & Guseva, N. G. 2021, MNRAS, 508, 2556
Izotov, Y. I., Thuan, T. X., & Privon, G. 2012, MNRAS, 427, 1229
Katz, H., Kimm, T., Ellis, R. S., Devriendt, J., & Slyz, A. 2023a, MNRAS, 524, 351
Katz, H., Saxena, A., Cameron, A. J., et al. 2023b, MNRAS, 518, 592
Kehrig, C., Guerrero, M. A., Vílchez, J. M., & Ramos-Larios, G. 2021, ApJL, 908, L54

Kehrig, C., Vílchez, J. M., Guerrero, M. A., et al. 2018, MNRAS, 480, 1081
Kehrig, C., Vílchez, J. M., Pérez-Montero, E., et al. 2015, ApJL, 801, L28
Kennicutt, R. C., & Evans, N. J. 2012, ARA&A, 50, 531
Kennicutt, R. C. J. 1998, ApJ, 498, 541
Kewley, L. J., Nicholls, D. C., & Sutherland, R. S. 2019, ARA&A, 57, 511
Korista, K., Ferland, G., & Baldwin, J. 1997, ApJ, 487, 555
Kormendy, J., & Ho, L. C. 2013, ARA&A, 51, 511
Kriek, M., van Dokkum, P. G., Labbé, I., et al. 2009, ApJ, 700, 221
Kudritzki, R.-P. 2000, in The First Stars, ed. A. Weiss, T. G. Abel, & V. Hill (Garching: Springer-Verlag), 127
Larson, R. L., Finkelstein, S. L., Kocevski, D. D., et al. 2023, arXiv:2303.08918
Lequeux, J., Peimbert, M., Rayo, J. F., Serrano, A., & Torres-Peimbert, S. 1979, A&A, 80, 155
Leung, G. C. K., Coil, A. L., Rupke, D. S. N., & Perrotta, S. 2021, ApJ, 914, 17
Levesque, E. M., & Richardson, M. L. A. 2014, ApJ, 780, 100
Maiolino, R., & Mannucci, F. 2019, A&ARv, 27, 3
Maiolino, R., Scholtz, J., Witstok, J., et al. 2023, arXiv:2305.12492
Maseda, M. V., van der Wel, A., da Cunha, E., et al. 2013, ApJL, 778, L22
Maseda, M. V., van der Wel, A., Rix, H.-W., et al. 2014, ApJ, 791, 17
Masters, D., McCarthy, P., Siana, B., et al. 2014, ApJ, 785, 153
Mehdipour, M., Kaastra, J. S., Kriss, G. A., et al. 2015, A&A, 575, A22
Mignoli, M., Vignali, C., Gilli, R., et al. 2013, A&A, 556, A29
Mitchell, J. A. J., Done, C., Ward, M. J., et al. 2023, MNRAS, 524, 1796
Nakamura, F., & Umemura, M. 2002, ApJ, 569, 549
Ohkubo, T., Nomoto, K., Umeda, H., Yoshida, N., & Tsuruta, S. 2009, ApJ, 706, 1184
Olivier, G. M., Berg, D. A., Chisholm, J., et al. 2022, ApJ, 938, 16
Papovich, C., Simons, R. C., Estrada-Carpenter, V., et al. 2022, ApJ, 937, 22
Pérez-Montero, E., Amorín, R., Sánchez Almeida, J., et al. 2021, MNRAS, 504, 1237
Peterson, B. M., Denney, K. D., De Rosa, G., et al. 2013, ApJ, 779, 109
Pontoppidan, K. M., Barrientes, J., Blome, C., et al. 2022, ApJL, 936, L14
Raiter, A., Schaerer, D., & Fosbury, R. A. E. 2010, A&A, 523, A64
Reback, J., Jbrockmendel, McKinney, W., et al. 2022, pandas-dev/pandas: Pandas v1.4.2, Zenodo, doi:10.5281/zenodo.3509134
Richards, G. T., Lacy, M., Storrie-Lombardi, L. J., et al. 2006, ApJS, 166, 470
Rigby, J. R., Bayliss, M. B., Gladders, M. D., et al. 2015, ApJL, 814, L6
Salpeter, E. E. 1955, ApJ, 121, 161
Schaerer, D. 2002, A&A, 382, 28
Senchyna, P., Stark, D. P., Mirocha, J., et al. 2020, MNRAS, 494, 941
Senchyna, P., Stark, D. P., Vidal-García, A., et al. 2017, MNRAS, 472, 2608
Simons, R. C., Papovich, C., Momcheva, I., et al. 2021, ApJ, 923, 203
Simons, R. C., Papovich, C., Momcheva, I. G., et al. 2023, ApJS, 266, 13
Smit, R., Bouwens, R. J., Labbé, I., et al. 2014, ApJ, 784, 58
Stanway, E. R., & Eldridge, J. J. 2018, MNRAS, 479, 75
Stark, D. P. 2016, ARA&A, 54, 761
Steidel, C. C., Rudie, G. C., Strom, A. L., et al. 2014, ApJ, 795, 165
Tan, J. C., & McKee, C. F. 2004, ApJ, 603, 383
Tang, M., Stark, D. P., Chevallard, J., et al. 2021, MNRAS, 501, 3238
Tang, M., Stark, D. P., Chevallard, J., & Charlot, S. 2019, MNRAS, 489, 2572
Trump, J. R., Arrabal Haro, P., Simons, R. C., et al. 2023, ApJ, 945, 35
Trump, J. R., Sun, M., Zeimann, G. R., et al. 2015, ApJ, 811, 26
Trussler, J. A. A., Conselice, C. J., Adams, N. J., et al. 2022, arXiv:2211.02038
Tumlinson, J. 2006, ApJ, 641, 1
van der Wel, A., Straughn, A. N., Rix, H. W., et al. 2011, ApJ, 742, 111
Vanden Berk, D. E., Richards, G. T., Bauer, A., et al. 2001, AJ, 122, 549
Veilleux, S., & Osterbrock, D. E. 1987, ApJS, 63, 295
Walter, R., & Fink, H. H. 1993, A&A, 274, 105
Waskom, M. 2021, JOSS, 6, 3021
Wuyts, S., Förster Schreiber, N. M., Lutz, D., et al. 2011, ApJ, 738, 106
Zackrisson, E., Rydberg, C.-E., Schaerer, D., Östlin, G., & Tuli, M. 2011, ApJ, 740, 13
Zeimann, G. R., Ciardullo, R., Gebhardt, H., et al. 2015, ApJ, 798, 29
Zheng, W., Kriss, G. A., Telfer, R. C., Grimes, J. P., & Davidsen, A. F. 1997, ApJ, 475, 469